Case Studies in Thermal Engineering 50 (2023) 103437

Contents lists available at ScienceDirect

Case Studies in Thermal Engineering

journal homepage: www.elsevier.com/locate/csite

Optimization design of space radiation cooler based on response surface method and genetic algorithm

Shuai Liu [a,b], Xu Meng [a,b], Zhipeng Yuan [a,b], Limin Ren [a,b], Liheng Chen [a,*]

[a] Changchun Institute of Optics, Fine Mechanics and Physics, Chinese Academy of Sciences, Changchun, Jilin, 130033, China
[b] University of Chinese Academy of Sciences, Beijing, China

ARTICLE INFO

Keywords:
Space radiator cooler
Space ultraviolet imager
Response surface method
Genetic algorithm optimization

ABSTRACT

The cooling capacity of a radiator under complex environmental conditions is improved by controlling the detector temperature within a range of the thermal control index. An optimal design method for the radiation cooler based on the response surface method (RSM) and genetic algorithm is proposed, and the area and location of the radiation cooler of the space ultraviolet imager detector are optimized. First, the physical model and thermal simulation model of the space ultraviolet imager are established. Then, the detector temperature is used as the objective function, and the length, height, and inclination angle of the radiator in space are used as the design variables. The mathematical model of the objective function is established by the RSM, and the rationality of the mathematical model is verified by analysis of variance (ANOVA). Finally, the Pareto optimal frontier is obtained using the genetic algorithm. The optimization results confirm that the optimal design parameters of the radiator are $X_W = 165.58$ mm, $X_H = 160.29$ mm, $\theta_1 = 7.28^\circ$, $\theta_2 = 5.87^\circ$. Compared with before optimization, the area of the radiator is reduced by 18.18%, and the weight is reduced by 48.78 g. Based on verifying the optimization results, the optimized radiation cooler can control the detector within the target temperature of -20 to -10 °C. Therefore, the optimal design of the radiation cooler meets the requirement of lightweight while improving the cooling capacity of the radiator.

1. Introduction

During the orbital operation of the spacecraft, the temperature of the internal working components fluctuates significantly because of the influence of the internal heat source and the heat flow outside space. It is necessary to control the internal components within a specific temperature range through thermal design. For cameras with space exploration missions, the thermal noise and dark current generated by the high detector temperature will reduce its imaging quality. Therefore, a special heat dissipation channel must be designed to dissipate the detector's heat. The radiation cooler is critical for dissipating the detector's heat into the 4 K space and must be specially designed to control the detector to a reasonable temperature.

Several researchers have studied radiant space coolers. Shen et al. [1] established the maximum thermal stiffness target of the radiator to improve the heat dissipation efficiency. Based on the OMEGA SSPS heat dissipation problem, Fan, G [2] proposed a thermal control method for space radiators based on the synchronous optimization of the shape and topology of the butterfly radiator. The optimal structural form is obtained by obtaining maximum heat dissipation at minimum mass and uniform boundary temperature. Cuco et al. [3] designed a new variable emittance radiator (VESPAR) that can save approximately 50% of heater power consumption.

---

[*] Corresponding author.
E-mail address: chenliheng3@163.com (L. Chen).

https://doi.org/10.1016/j.csite.2023.103437
Received 7 June 2023; Received in revised form 25 July 2023; Accepted 29 August 2023

VESPAR is heavier than traditional space radiators and unsuitable for loads with strict lightweight requirements. Sam and Deng [4] embedded heat pipes in the heat sink, improving the heat dissipation efficiency of the radiator but increasing the weight by 7.37 kg. The length of the heat pipe was then used as the optimization design variable, and the minimum total weight of the heat pipe network was optimized as the objective function.

Kim et al. [5] proposed two optimal design methods for heat sinks based on thermal model node division. These methods solve the optimal solution for the combination of heat sink nodes differently. The first method uses integrated optimization analysis, combining optimization algorithms with thermal analysis (TA). The second method gradually increases the heat sink node based on temperature sensitivity until the temperature limit is met. Bulut and Sözbir [6] determined the emitter area according to the maximum temperature of the load (end of life) and optimized it at low temperature (early stage of life). Bulut and Sözbir [7] developed a practical emitter TA tool (PLTAT) based on Excel's VBA user interface. The heat dissipation values of the different panel sizes of the satellite are calculated by PLTAT to determine the radiator area. Vilela and Garcia [8] proposed a numerical model to analyze the critical working conditions of space radiators and conducted numerical simulations of finned space radiators on the surface of satellites to evaluate the temperature distribution of radiators under extreme working conditions. This model can optimize the number and size of radiator fins. Arslanturk [9] used the parameter change method (VPM) to solve the nonlinear and non-homogeneous differential equations and used the classical search method to determine the optimal size of the space heat sink.

This optimized radiation cooler design can improve the heat dissipation efficiency of the radiator. However, there is little or no occlusion in the heat dissipation direction of the radiator. When the radiation cooler is seriously blocked, this optimization method cannot improve the radiation cooler's heat dissipation capacity.

The radiator optimally designed in this study is used to cool the detector of a space ultraviolet imager. It satisfies the thermal control index of the detector and lightweight requirements. The space environment where the radiation cooler is located is complex and is blocked by other satellite components, making it difficult for the radiator to dissipate heat. Furthermore, it is difficult to dissipate the heat inside the detector into the cold and 4 K space.

In this study, the physical model and thermal simulation model of the space ultraviolet imager are established. According to the limited space position, the detector temperature is used as the objective function, and the radiator's length, height, and inclination angle in space are used as design variables. Design of experiments and response surface methods (RSMs) were used to fit the response surface-regression model of the detector temperature to the design variables of the radiator. The practicability of the regression model was verified by variance analysis. Finally, the objective function is optimized using the multi-objective genetic algorithm (MOGA), the optimal design front is obtained by the Pareto optimal solution, and the optimal design parameters of the radiator that can reduce the detector temperature to the thermal control index are obtained.

2. Physical model

2.1. Description of ultraviolet imager on-orbit operation

The ultraviolet imager is installed on the connecting frame between the satellite and the solar panel. The attitude adjustment mechanism of the solar panel is used to make the light entrance of the imager always point to the Sun, and the sunlight directly enters the optical port through the attitude adjustment mechanism of the ultraviolet imager. The satellite runs in the geostationary orbit, and the satellite is always facing the Earth. The solar panel and the connecting frame need to rotate at a speed of 0.25°/min to ensure that the imager continues to point to the Sun. The installation location and on-orbit situation of the ultraviolet imager are depicted in Fig. 1. The β angle (the angle between the Sun vector and the orbital plane) changes caused by the revolution of the Earth. The change rule is depicted in Fig. 2. Therefore, if direct sunlight is guaranteed to enter the optical port, the imager must also be pitched -23.5° to $+23.5^\circ$/year with the change in the β angle. The schematic of pitching is depicted in Fig. 3. Two extreme working conditions are defined according to the on-orbit working conditions of the imager (Table 1).

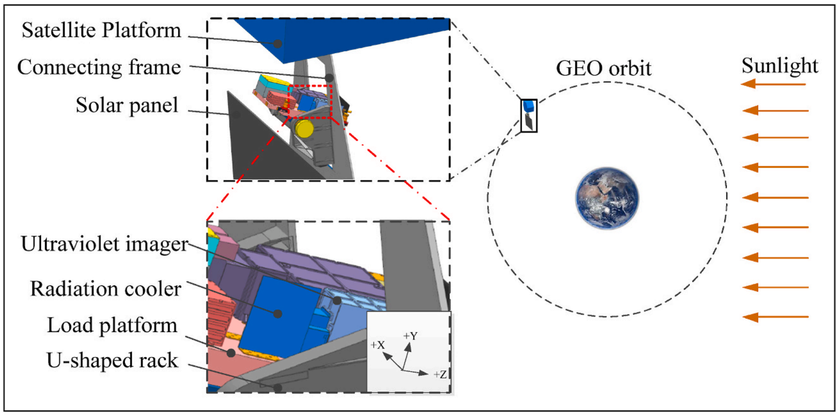

Fig. 1. Ultraviolet imager installation location and on-orbit diagram.

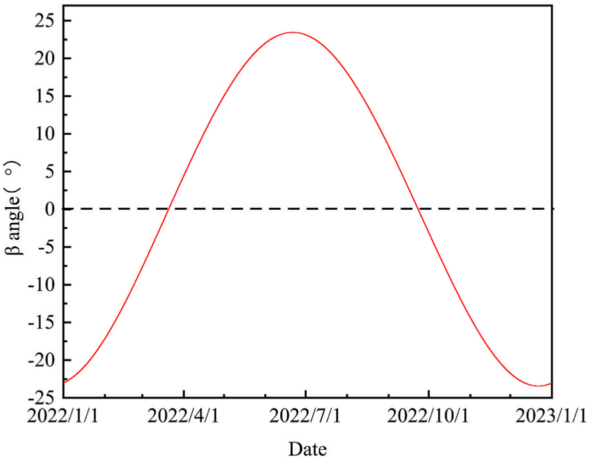

Fig. 2. Annual variation law of β angle.

2.2. *Ultraviolet imager radiation cooler working environment*

The detector temperature is controlled within a range of −20 to −10 °C through the radiation cooler and heater to ensure the imaging performance of the imager detector. Given the spatial position of the imager, the radiation cooler can only dissipate heat in the -X direction; the position of the radiator is depicted in Fig. 1. With the attitude adjustment of the imager, the radiator has more occlusions in the -X direction, such as the turntable, connecting frame, and satellite. Furthermore, the maximum temperature of the connection frame reaches 65 °C, which affects the radiator and a particular amount of radiation heat exchange, reducing the cooling capacity of the radiation cooler. Therefore, the research purpose of this study is to improve the cooling capacity of the radiation cooler by optimizing the area and position of the radiation cooler.

2.3. *Heat transfer model of detector assembly*

Fig. 4 illustrates the structure diagram of each part of the detector assembly. The heat transfer path of the detector assembly can be determined according to Figs. 1 and 2. A schematic of the thermal balance of the detector assembly is depicted in Fig. 5. R1–R8 are the thermal resistances between the assemblies. According to Fig. 5 and the law of conservation of energy, the heat balance equation of the radiation cooler is established as follows:

$$Q_1 + \sum_{i=2}^{6} Q_{ir} + Q_7 = Q_8 + Q_9 \tag{1}$$

where Q_1 is the external heat flow absorbed by the radiant space cooler, Q_{2r} is the heat given to the radiator by the star platform, Q_{3r} is the heat from the connection frame to the radiator, Q_{4r} is the heat from the load platform to the radiator, Q_{5r} is the heat supplied by the U-shaped frame to the radiator, Q_{6r} is the heat supplied by the solar panel to the radiator, Q_7 is the heat transferred from the detector to the radiator through thermal conduction, Q_8 is the radiation heat exchange between the radiator and the 4 K space, and Q_9 is the change in the internal energy of the radiator.

The radiant heat flow of the space environment received by the radiator can be calculated by Equation (2). The heat transferred from the remaining surfaces to the radiator by radiation is calculated by Equation (3). The heat conducted by the detector to the radiator through heat can be calculated by Equation (4). The radiant heat transfer between the radiator and the 4 K space is calculated

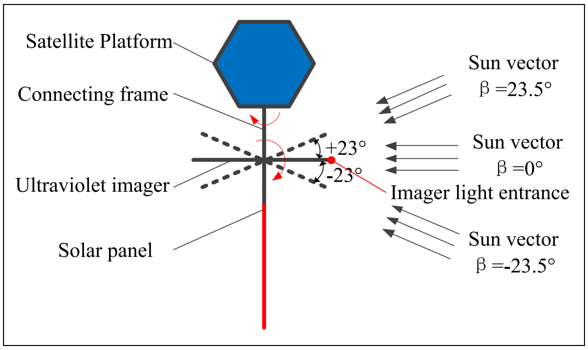

Fig. 3. Ultraviolet Imager pitch angle and Sun vector diagram.

Table 1
Definition of extreme working conditions during on-orbit operation.

Name	High-Temperature Condition	Low-Temperature Condition
Solar constant (W/m^2)	1323	1412
Detector power (W) Consumption	0.5	0.5
β angle (°)	−23.5	23.5
Pitching angle (°)	−23.5	23.5
Satellite platform temperature (°C)	30	−20
Satellite platform α_s/ε	0.25/0.8	0.1/0.8
Radiation cooler α_s/ε	0.35/0.86	0.17/0.86
Multilayer thermal Insulation components α_s/ε	0.36/0.69	0.37/0.69
Connection frame α_s/ε	0.55/0.86	0.23/0.86
Solar panel α_s/ε	0.93/0.86	0.93/0.86

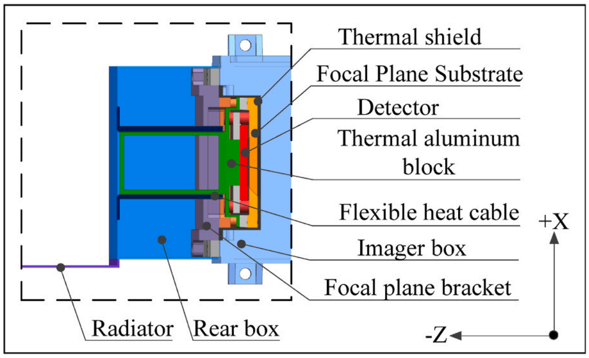

Fig. 4. Detector component installation relationship.

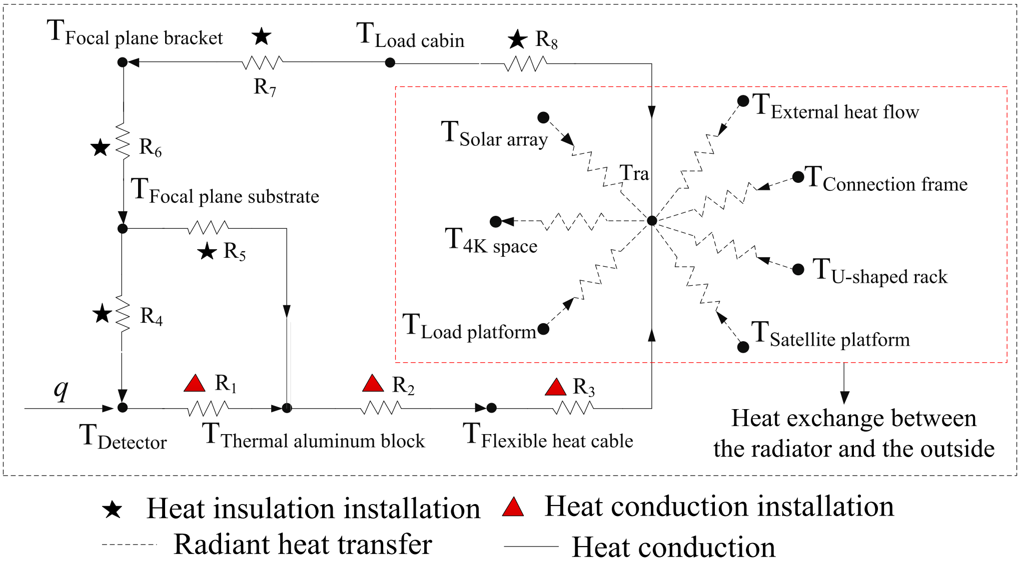

Fig. 5. Schematic of thermal balance of detector components.

by Equation (5). The amount of change in the internal energy of the radiator is calculated by Equation (7).

$$Q_1 = \left(\alpha_s S_0 \varphi_1 + \alpha_s S_0 \varphi_2 R + \varepsilon_1 \frac{(1-R)}{4} S_0 \varphi_3\right) A \tag{2}$$

$$Q_{ir} = A_i F_{i,r} (J_i - J_r) \tag{3}$$

$$Q_7 = \frac{T_D - T_Z}{\sum \frac{1}{kA_s} + \sum \frac{d_j}{\lambda_j A_j}} \tag{4}$$

$$Q_8 = \sigma \varepsilon_1 A_1 F_{1,2} \left(T_1^4 - T_2^4 \right) \tag{5}$$

$$F_{1,2} = \int_{A_1} \left(\int_{A_2} \frac{cos\ \theta_1\ cos\ \theta_2 dA_2}{\pi r^2} \right) dA_1 \tag{6}$$

$$Q_9 = \sum \left(m_i c_i \frac{\partial T}{\partial \tau} \right) \tag{7}$$

where α_s is the solar absorptivity on the surface of the radiation cooler, the solar constant S_0 is 1411 W/m^2,φ_1 is the angle factor of the radiation cooler to the direct solar radiation, φ_2 is the angular coefficient of the radiation cooler surface to the Earth's albedo radiation, R is the average reflectivity of the ground, φ_3 is the Earth's infrared angle coefficient, ε_1 is the infrared emissivity of the radiator surface, A_i is the area of the star platform, the connecting frame, the load platform, the U-frame and the solar panel, respectively, $F_{i,r}$ is the viewing angle coefficient of the star platform, the connecting frame, the load platform, the U-frame and the solar panel to the radiator, respectively, J_i is the effective radiation of star platform, connecting frame, load platform, U-frame, and solar panel, J_r is the effective radiation of the radiator, T_D is the detector temperature, T_Z is the radiation cooler temperature, k is the thermal conductivity, A_s is the contact area of the two components, d_j is the thickness of a single heat transfer component, λ_j is the thermal conductivity of a single component material, A_j is the cross-sectional area of the component perpendicular to the heat flow transfer direction, σ is the Stefan-Boltzmann constant, T_1 is the surface temperature of the radiation cooler, T_2 is the space ambient temperature, A_1 is the surface area of the radiation cooler, m_i is the radiator mass, c_i is the specific heat capacity of the radiation cooler, $\partial T/\partial \tau$ is the temperature change rate of the radiation cooler, dA_1 is the micro-element area of the radiation cooler, and dA_2 is the micro-element area that blocks the radiation cooler. The remaining parameters of Equation (6) are depicted in Fig. 6.

According to Equations (3), (5) and (6) and Fig. 6, the radiation heat transfer between the two surfaces is related to the relative position between the two surfaces and the area of the two surfaces. In the following optimization design process, the width X_W of the radiator, the height of the radiator X_H, and the inclination angle θ of the radiation cooler are used as design variables, and the detector

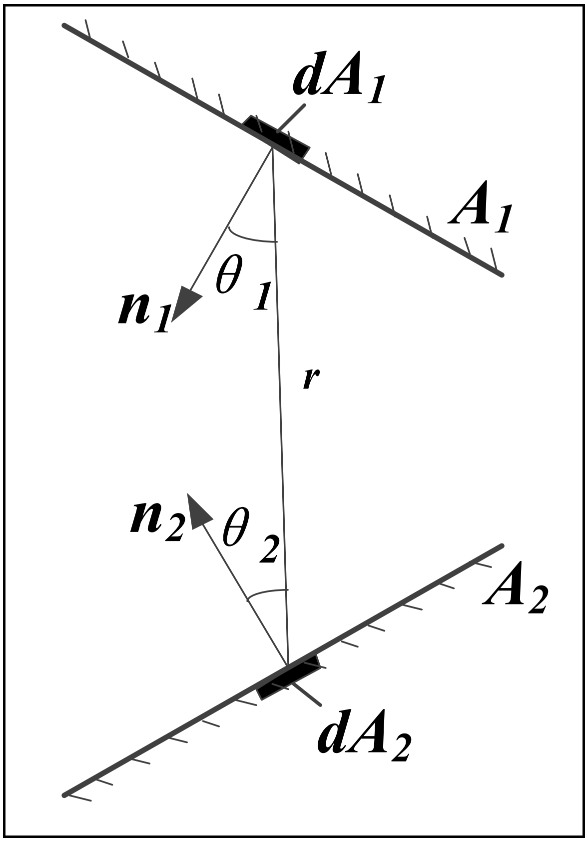

Fig. 6. Parameters from Equation (6).

temperature and the area of the radiation cooler are used as the objective function for optimization.

3. Optimization process

In this section, the RSM is used to determine the effect of the radiator area and location on the temperature of the ultraviolet imager detector. The response surface numerical model required for optimization was developed based on experimental design and regression analysis.

Fig. 7 illustrates the optimization design flow of RSM and MOGA. First, for the specific optimization design problem, the design and target variables are determined according to the actual conditions. Second, the RSM based on the Box–Behnken experimental design is used to construct a quadratic mathematical model between the design variable and the target variable; the rationality of the mathematical model is verified by analysis of variance (ANOVA). Finally, the MOGA is used to solve the optimization problem.

3.1. Design variables and objective function

According to Equations (3), (5) and (6), by changing the relative position and area of the radiator in space, the heat dissipation capacity of the radiation cooler can be changed to further reduce the detector temperature within the target range.

The position of the radiation cooler can be determined by four design parameters: radiator width X_W, radiator height X_H, radiator rotation angle θ_1 around the Y axis, and radiator rotation angle θ_2 around line L (Fig. 8). The four design parameters that determine the location of the radiation cooler are the design variables. The detector temperature and area of the radiation cooler are used as objective functions.

3.2. Experimental design

The RSM [10–13] is an experimental method to explore the relationship between multiple design variables and one or more response variables. It is also one of the most widely used and effective methods for solving optimization problems in engineering analysis and optimization design. Based on different methods of selecting experimental points [14], RSM can be divided into a full-factorial design, orthogonal array, center combination design, Box–Benken design, Latin hypercube design, optimal Latin hypercube design, and other methods. The Box–Benken design consists of multiple orthogonal cubes and contains a center point. Because it avoids the appearance of extreme points [15], it can be applied to optimizing mechanical dimensions. There is no situation where a particular size is too small such that the test is impossible or the results unstable. Therefore, the Box–Benken design method is used to select the test points required by the RSM.

Each optimization parameter is designed with three levels. A total of 29 groups of tests are required, and the finite element method is used to calculate the detector temperature corresponding to different parameters. There are various forms of surrogate models

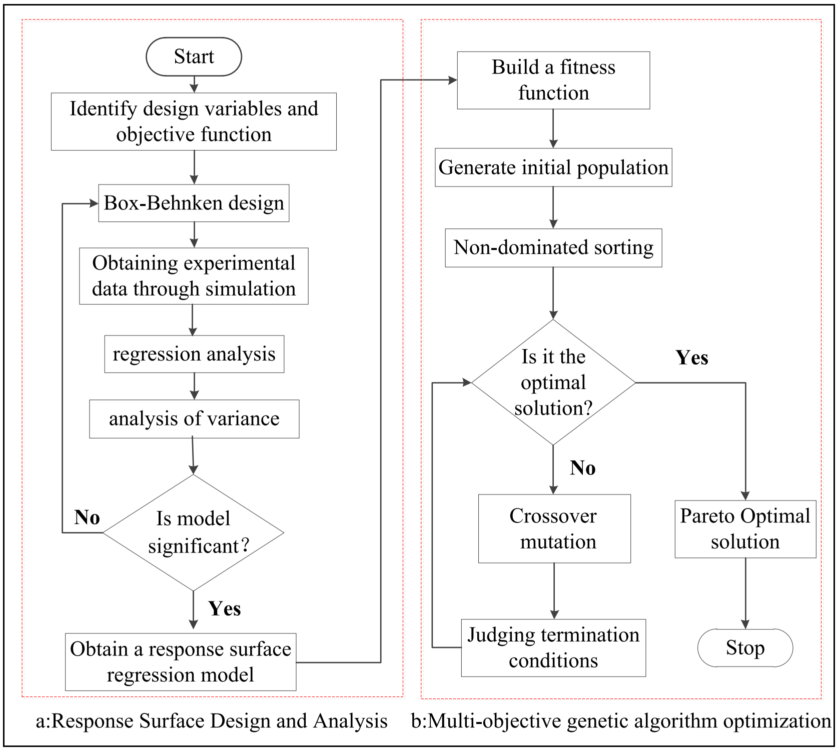

Fig. 7. Flow chart of optimal design of DOE, RSM, and MOGA.

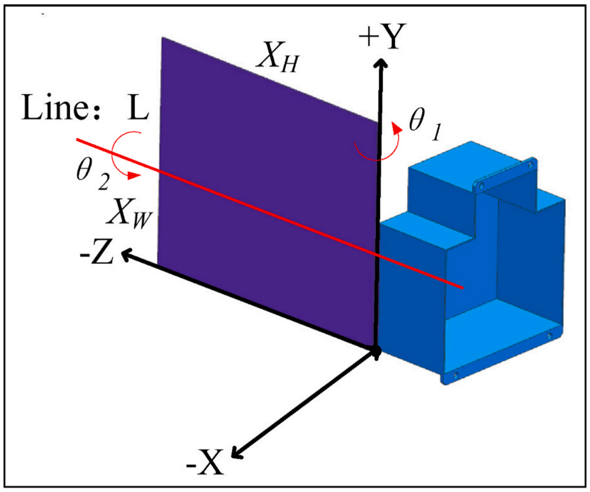

Fig. 8. Schematic of radiator parameters.

obtained through RSMs, but the most common models are polynomials based on Taylor expansions, calculated as follows [16]:

$$Y=\beta_0+\sum_{i=1}^{k}\beta_i x_i+\sum_{i=1}^{k}\beta_{ii}x_i^2+\sum_{i=1}^{k-1}\sum_{j=2}^{k}\beta_{ij}x_i x_j+\varepsilon \tag{8}$$

where β_0 is the model constant, β_i is the linear coefficient, β_{ii} represents the quadratic coefficient, β_{ij} is the interaction coefficient, k is the number of factors or variables, ε is the model residual, β_i. β_{ii} and β_{ij} are collectively referred to as unknown parameters, and Y is the response item. The value of the response variable is obtained using real-world or simulated experiments. Then, the approximation function between the responses can also be written in matrix form based on the model terms of the quadratic polynomial model as follows:

$$Y=X\beta+\varepsilon \tag{9}$$

where X is a matrix of model terms, including linear terms, square terms, and interaction terms, β is a column vector containing the undetermined coefficients, and ε is the residual vector.

3.3. *Model diagnostics*

ANOVA was used to assess the suitability and significance of the proposed model. In this analysis, F- and *P*-values were used to assess the validity of the regression model and the effect of each factor combination on the model. Smaller p-values (or larger F-values) indicate a more significant model, and terms with p-values less than 0.05 are considered significant. In terms of model fitness, the coefficient of determination, including three crucial indicators R^2, R2 adj, and R2 pre in a range of 0–1; the closer the value is to 1, the higher the fitness [17].

$$R^2=1-\sum_{i=1}^{n}(y_i-\hat{y}_i)^2\bigg/\sum_{i=1}^{n}(y_i-\bar{y})^2 \tag{10}$$

$$R_{adj}^2=1-\left(\sum_{i=1}^{n}(y_i-\hat{y}_i)^2\bigg/(n-p)\right)\bigg/\left(\sum_{i=1}^{n}(y_i-\bar{y})^2\bigg/(n-1)\right) \tag{11}$$

$$R_{pre}^2=1-\sum_{i=1}^{n}\left(\frac{y_i-\hat{y}_i}{1-h_{ii}}\right)^2\bigg/\sum_{i=1}^{n}(y_i-\bar{y})^2 \tag{12}$$

where n-p is the degrees of freedom of the model residuals, n-1 is the total corrected degrees of freedom, and h_{ii} is the ith diagonal element of $H=X(X^TX)^{-1}X^T$ [18].

3.4. *Multi-objective genetic algorithm (MOGA)*

Multi-objective optimization refers to solving problems with multiple design objectives. In many practical engineering problems, there may be conflicts among multiple design goals. When one design goal is optimal, the other design goals are not optimal. Therefore, the term "optimization" in multi-objective problems usually refers to finding a set of non-inferior solution points [19]. Designers only need to select the final solution from the Pareto set according to the engineering needs.

MOGA can solve various multi-objective optimization problems and obtain optimal Pareto solutions. Researchers can select the required optimal solutions from the Pareto optimal solutions according to the project's needs. Compared with other optimization methods, MOGA randomly searches the space based on the information obtained from the evolutionary process, which can reduce the probability of falling into the local optimal solution—the algorithm is easy to implement after long-term development [20]. The optimization flow chart is depicted in Fig. 7b. The design parameters of MOGA are as follows: population size of 200, generations of 300, Crossover Fraction of 0.8, Pareto frontier population score of 0.3, StallGenLimit of 500, and function tolerance of 10^{-10}.

The radiator area and detector temperature are the two objective functions in this study. The goal of optimization is to minimize the area of the radiator while minimizing the detector temperature. The four design parameters of the optimization process are the length of the radiator, the length of the width of the radiator, the rotation angle of the radiator around line L and the rotation angle of the radiator around the Y axis. In practical design studies, a range of design variables is determined according to the limited space in which the radiator is located. The optimization problem can be expressed by Equation (13).

$$\begin{cases} \text{Find}: X_W, X_H, \theta_1, \theta_2 \\ \text{Minimize}: T_D(X_W, X_H, \theta_1, \theta_2), S(X_W, X_H) \\ \text{Within ranges}: 0.13m \le X_W \le 0.2m, 0^\circ \le \theta_1 \le 14^\circ \\ 0.10m \le X_H \le 0.165m, -12^\circ \le \theta_2 \le 6^\circ \end{cases} \tag{13}$$

The relative error of the detector temperature before and after optimization can be calculated as follows:

$$error = (T_{TA} - T_{MOGA}) / T_{TA} \tag{14}$$

The weight of the radiator is calculated as follows:

$$m = \rho X_W X_H d \tag{15}$$

where ρ is the density of the radiator, the radiator is made of aluminum alloy, ρ is 2710 kg/m^3, d is the thickness of the radiator, the thickness remains unchanged before and after optimization, and d is 0.003 m.

4. Results and discussion

4.1. Numerical experimental design

In this study, a Box–Behnken design with four factors and three levels was conducted, and a range of design parameters was confirmed according to the spatial location of the radiators and engineering analysis. The height of the radiator cannot exceed the height of the imager because of the outer contour of the imager. The height of the radiator cannot exceed 0.165 m. According to the simulation calculation, the height of the radiator cannot be lower than 0.1 m, so this value range is 0.1–0.165 m. On the basis of the distribution of the imager and the rest of the load on the mounting substrate, the length of the radiator should not exceed 0.2 m. Similarly, on the basis of the simulation calculation, the excess length of the radiator should not be less than 0.13 m, so its value range is 0.13–0.2 m. Furthermore, considering the actual situation of on-orbit operation, a larger turning angle will cause the radiator to be exposed to the Sun. A smaller turning angle will reduce the viewing angle coefficient of the radiator toward the cool and dark space, reducing the cooling capacity of the radiator. Therefore, the value ranges of θ_1 and θ_2 are 0–14° and -12–6°. Fig. 9 shows the thermal analysis model relevant to the experimental design. Table 2 shows the Box–Behnken experimental design and computational results.

4.2. Analysis of variance (ANOVA)

The residual normal probability plot of the detector temperature is depicted in Fig. 10. The detector temperature residual points are

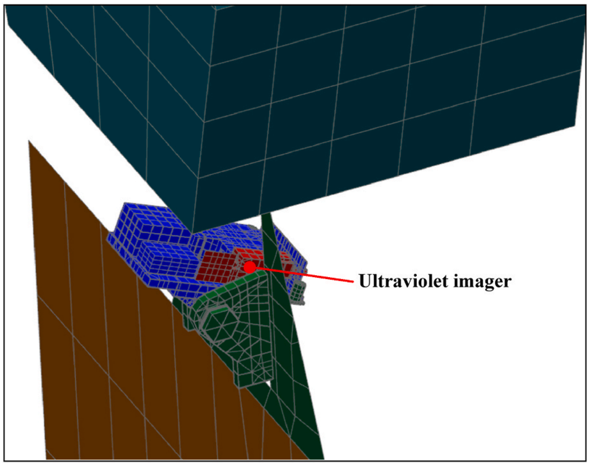

Fig. 9. TA model.

Table 2
Box–Behnken experimental design and computational results.

experiment No.	Variable				Response
	X_W (mm)	X_H (mm)	θ_1 (°)	θ_2 (°)	T_D (°C)
1	0.165	0.1650	0	−3	−18.167
2	0.130	0.1325	7	−12	−9.689
3	0.165	0.1650	7	−12	−16.19
4	0.165	0.1325	0	6	−16.545
5	0.130	0.1325	0	−3	−10.779
6	0.165	0.1325	0	−12	−12.468
7	0.130	0.1000	7	−3	−5.123
8	0.165	0.1000	14	−3	−8.955
9	0.165	0.1000	7	−12	−8.407
10	0.200	0.1650	7	−3	−20.87
11	0.165	0.1650	7	6	−20.744
12	0.165	0.1325	7	−3	−14.822
13	0.165	0.1325	7	−3	−14.822
14	0.165	0.1325	7	−3	−14.822
15	0.200	0.1325	7	6	−19.18
16	0.165	0.1325	7	−3	−14.822
17	0.200	0.1325	0	−3	−17.921
18	0.165	0.1000	0	−3	−9.765
19	0.130	0.1325	7	6	−12.874
20	0.200	0.1000	7	−3	−11.95
21	0.130	0.1325	14	−3	−11.992
22	0.165	0.1325	14	6	−16.633
23	0.165	0.1000	7	6	−9.696
24	0.200	0.1325	7	−12	−15.698
25	0.130	0.1650	7	−3	−15.123
26	0.165	0.1325	14	−12	−13.111
27	0.200	0.1325	14	−3	−17.116
28	0.165	0.1650	14	−3	−18.229
29	0.165	0.1325	7	−3	−15.133

located on both sides of the straight line, indicating that the detector temperature residual points obey a normal distribution. Fig. 11 compares the results from the experimental data with those predicted by RSM. The predicted value is consistent with the distribution law of the experimental value, which is roughly on the same straight line, which verifies the accuracy of the regression.

ANOVA is used to test the significance of quadratic model terms. On the basis of Table 3, the F-value of the detector temperature model is 383.26, indicating that the equation model is highly significant. The difference between the corrected complex correlation coefficient and the predicted complex correlation coefficient is small ($R^2 = 0.9974$, R2 adj = 0.9948, R2 pre = 0.9858), and both are close to 1, indicating that the equation model does not require further optimization. The linear terms X_W, X_H, and θ_2 in this equation model are significant ($P < 0.05$), and the quadratic terms $X_W\theta_1$, $X_H\theta_2$, $X\,2\,W$, and $X\,2\,H$ are highly significant ($P < 0.01$), indicating that each factor affects the detector temperature in addition to its own, with distinct interactions between them. A coefficient of variation in 1.97% < 15% indicates that all experimental data have no significant abnormality. The lack of fit is not significant ($P > 0.05$), indicating that the regression equation fits well, and the model is stable.

The results of variance analysis demonstrate that the model can fit the experimental results well, so the regression model can be used to analyze the relationship between factors and obtain the optimal combination of factors. Then, the objective function will be optimized next using the MOGA to continue the optimization process.

4.3. Regression model

On the basis of the experimental results in Table 3, the regression response surface model with respect to the detector temperature is fitted based on Equation (16), which is the fitted quadratic polynomial model, and Table 4 presents the coefficients of each item.

$$T_D = a + bX_W + cX_H + d\theta_1 + e\theta_2 + fX_WX_H + gX_W\theta_1 + hX_W\theta_2 + iX_H\theta_1 + jX_H\theta_2 + k\theta_1\theta_2 + lX_W{}^2 + mX_H{}^2 + n\theta_1{}^2 + o\theta_2{}^2 \tag{16}$$

Equation (16) is optimized using the MOGA, and the Pareto fronts for obtaining detector temperature and radiator area are plotted in Fig. 12. Because the temperature index of the detector is −20 to −10 °C, each point in the dotted line in Fig. 12 is the optimal design value. The optimal point is typically chosen based on the radiator area and the temperature requirements of the detector. The thermal control index of the detector is −20 to −10 °C, so the optimal solution that satisfies the thermal control index can be selected within a range of the dotted line in the figure. Table 5 presents the optimal point within the dotted line in detail.

The entire optimization process is intended to optimize the radiator under high-temperature conditions to verify that the radiator can dissipate heat and lower the detector temperature to a range of −20 °C. Under low-temperature conditions, the radiator can also reduce the detector temperature to −20 °C, or even lower than −20 °C, so that the temperature can be controlled within the target range using active heating. On the basis of Table 5, when the detector temperature is around −10 °C, the area of the radiator may be the smallest relative to the entire Pareto optimal solution set. Given various uncertain factors in the design, corresponding design errors

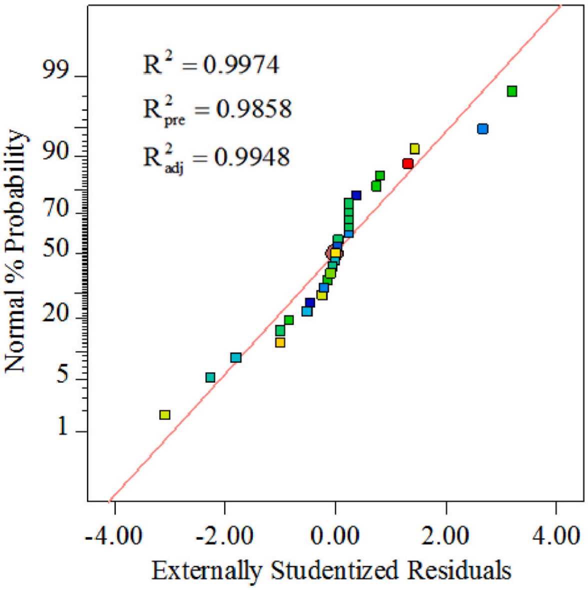

Fig. 10. Normal distribution plot of residuals.

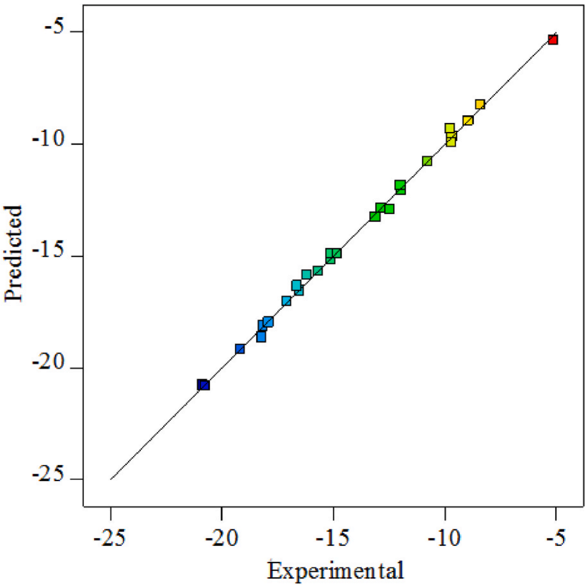

Fig. 11. Distribution of predicted and experimental values.

may be caused. For example, the actual contact thermal resistance is inconsistent with the design value because of installation or processing. The tightness of the multilayer thermal insulation material is not easy to control. It is necessary to leave a sufficient design margin within the temperature specification range. Therefore, a detector temperature of approximately −20 °C is selected as the optimal design value for the radiator.

4.4. Multi-objective optimization

Table 6 lists the optimization results and the relative errors of the simulation results for the three cases selected from Table 5. On the basis of Table 6, the detector temperature for Case 3 is closest to the cryogenic requirement (−20 °C). Therefore, the area of the radiator is determined to be 0.027 m^2, the width of the radiator is $X_W = 165.58$ mm, the height $X_H = 160.29$ mm, and the inclination angle $\theta_1 = 7.28^\circ$, the inclination angle $\theta_2 = 5.87^\circ$.

Operation of the detector at low temperatures requires increasing the compensated heating power consumption of the detector and controlling the detector temperature above −20 °C. Simultaneously, to verify the heating ability to compensate for the heating power

Table 3
ANOVA results of detector-temperature response surface-regression model.

Source	Sum of squares	DOF	Mean square	F-value	*P*-value
Model	417.58	14	29.83	383.26	<0.0001
X_W	115.04	1	115.04	1478.19	<0.0001
X_H	256.01	1	256.01	3289.57	<0.0001
θ_1	0.0127	1	0.0127	0.1637	0.6919
θ_2	33.70	1	33.70	432.99	<0.0001
X_WX_H	0.2916	1	0.2916	3.75	0.0734
$X_W\theta_1$	1.02	1	1.02	13.08	0.0028
$X_W\theta_2$	0.0221	1	0.0221	0.2834	0.6029
$X_H\theta_1$	0.1901	1	0.1901	2.44	0.1404
$X_H\theta_2$	2.67	1	2.67	34.24	<0.0001
$\theta_1\theta_2$	0.0770	1	0.0770	0.9895	0.3368
X 2 W	1.34	1	1.34	17.16	0.0010
X 2 H	7.72	1	7.72	99.16	<0.0001
θ_1^2	0.0071	1	0.0071	0.0909	0.7675
θ_2^2	0.0511	1	0.0511	0.6567	0.4313
Residual	1.02	14	0.0726	–	–
Lack of Fit	1.01	10	0.1012	5.23	0.0624
Total	420.7	28	–	–	–

Table 4
Coefficients of quadratic polynomial terms.

Coefficient	Value	Coefficient	Value
a	54.133569270576	*i*	−0.95824175824176
b	−257.27544740974	*j*	−2.7905982905983
c	−456.6092533108	*k*	0.002202380952381
d	−0.22027922553637	*l*	370.42176870749
e	0.21361132817799	*m*	1032.6785009862
f	237.36263736266	*n*	0.00067380952380937
g	2.0591836734694	*o*	0.0010958847736625
h	−0.23571428571428		

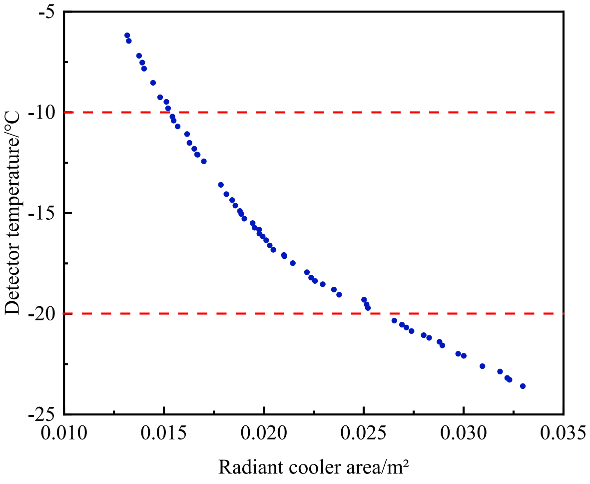

Fig. 12. Pareto optimization frontier for MOGA.

consumption, the detector temperature must be increased to −10 °C. Table 7 compares the design parameters obtained based on experience and the optimized parameters. After optimization, the area required to reduce the temperature to −20 °C under high-temperature conditions is reduced by 18.18%, and the weight is reduced by 48.78 g. Under the low-temperature condition, the heating power consumption required to control the detector temperature to −10 °C is only 0.81% higher than before optimization.

5. Conclusion

The purpose of this study is to optimize the design of the area and space of the radiant cooler, to increase the cooling capacity of the radiant cooler, and then control the detector temperature within a range of −20 to −10 °C. Numerical relationships between design

Table 5
Optimal points for multi-objective optimization.

X_W (m)	X_H (m)	θ_1 (°)	θ_2 (°)	S (m^2)	T_D (°C)
0.131487	0.117359	10.26515	5.68273	0.015431	−10.2165
0.131051	0.118192	12.14575	5.687517	0.015489	−10.4091
0.131218	0.119593	11.76255	5.6742	0.015693	−10.7025
0.135038	0.119703	10.13475	5.617266	0.016164	−11.0802
0.131887	0.12345	10.83462	5.654252	0.016282	−11.5132
0.131354	0.125801	9.051457	5.493463	0.016524	−11.8099
0.131918	0.126339	11.42733	5.611025	0.016666	−12.0948
0.131406	0.127014	10.6169	5.393031	0.01669	−12.1026
0.134648	0.126279	12.53906	5.751009	0.017003	−12.4315
0.133289	0.133966	9.768367	5.873613	0.017856	−13.5977
0.132485	0.136847	11.32434	5.761183	0.01813	−14.0659
0.132941	0.138533	10.80115	5.686702	0.018417	−14.3566
0.131845	0.140907	11.24307	5.564189	0.018578	−14.6316
0.132182	0.142274	11.46637	5.595258	0.018806	−14.9025
0.13229	0.142692	12.05513	5.798812	0.018877	−15.0486
0.131623	0.144577	12.37804	5.721148	0.01903	−15.2802
0.133224	0.145938	10.21986	5.608716	0.019442	−15.5029
0.131487	0.148609	10.26515	5.68273	0.01954	−15.7301
0.135541	0.145868	11.37088	5.765487	0.019771	−15.8237
0.132087	0.149737	11.64979	5.570378	0.019778	−16.0212
0.132226	0.150837	11.03653	5.629989	0.019944	−16.163
0.13377	0.150407	12.23599	5.7248	0.02012	−16.3514
0.132245	0.153495	11.74755	5.801248	0.020299	−16.6131
0.131652	0.155548	12.29418	5.615114	0.020478	−16.8265
0.133273	0.157637	10.45047	5.425405	0.021009	−17.0855
0.13448	0.156416	10.95791	5.707532	0.021035	−17.149
0.135985	0.157765	11.1311	5.754534	0.021454	−17.4894
0.138275	0.160267	9.801732	5.782926	0.022161	−17.94
0.137147	0.163138	9.795562	5.97172	0.022374	−18.2057
0.139098	0.162235	11.73108	5.800101	0.022567	−18.3725
0.140556	0.163288	10.57439	5.699535	0.022951	−18.5349
0.145678	0.161392	10.73385	5.712715	0.023511	−18.8034
0.145959	0.162887	11.25945	5.844858	0.023775	−19.055
0.160266	0.156135	2.701376	5.819544	0.025023	−19.3065
0.157106	0.160058	7.368135	5.666771	0.025146	−19.5388
0.155584	0.16206	8.90513	5.827677	0.025214	−19.7104
0.16558	0.16027	7.27615	5.86992	0.02654	−20.339

Table 6
Optimization results and TA calculation results.

	X_W (m)	X_H (m)	θ_1 (°)	θ_2 (°)	TA (°C)	MOGA (°C)	Error
Case1	0.15711	0.16006	7.37	5.67	−18.59	−19.54	5.11%
Case2	0.15558	0.16206	8.91	5.83	−18.87	−19.71	4.45%
Case3	0.16558	0.16029	7.28	5.87	−19.72	−20.34	3.14%

Table 7
Comparison of optimized design and experiential design results.

		Experiential design	Optimal design	Error
Design parameter	X_W(m)	0.2	0.16558	–
	X_H(m)	0.165	0.16029	–
	θ_1 (°)	0	7.28	–
	θ_2 (°)	0	5.87	–
Result	T_D (°C)	−20.81	−19.72	–
	S (m^2)	0.033	0.027	18.18%
	W (g)	268.29	219.51	48.78
	P (W)	2.45	2.47	0.82%

parameters and response variables were investigated using an RSM based on the design of experiments and numerical experiments. ANOVA was used to determine the accuracy of the detector temperature regression model, and the regression coefficient was greater than 0.9, indicating that the fitted regression model had high accuracy. The genetic algorithm is used to optimize the regression model. The optimization result is expressed in the form of a Pareto front. The optimal design point of the radiator is selected based on the low weight requirements of the load and the temperature requirements of the detector. The optimal size is width $X_W = 165.58$ mm, height

$X_H = 160.29$ mm, inclination angle $\theta_1 = 7.28^\circ$, and inclination angle $\theta_2 = 5.87^\circ$.

Compared with before optimization, the area of the radiator after optimization is reduced by 18.18%, the weight is reduced by 48.78 g, and the active heating power consumption is only increased by 0.82%. The optimized radiator can reduce the detector temperature to -20 °C under high-temperature conditions and heat the detector to -10 °C using compensation heating under low-temperature conditions. This finding confirms that the optimal design of the radiator combined with the response surface and genetic algorithm can control the detector temperature in a range of -20 to -10 °C, satisfying the thermal control index. The optimal design method of the radiator proposed in this paper provides a critical reference for the design of the radiator in a complex space environment. In the Pareto optimal solution set, designers can choose the appropriate optimal value according to the actual design requirements.

Author statement

Shuai Liu: Conceptualization, Methodology, Validation, Formal analysis, Investigation, Writing-original draft. **Meng Xu:** Writing-review & editing, Visualization. **Zhipeng Yuan:** Validation, Formal analysis, Visualization. **Limin Ren:** Formal analysis, Visualization. **Liheng Chen:** Methodology, Writing review & editing, Supervision, Project administration, Funding acquisition.

Declaration of competing interest

No conflict of interest exists in the submission of this manuscript, and the manuscript is approved by all authors for publication.

Data availability

No data was used for the research described in the article.

Acknowledgments

This work was supported by The National Key Research and Development Program of China (No.2021YFB3901000, 2021YFB3901004).

We thank Philip Pape, PhD, from Liwen Bianji (Edanz) (www.liwenbianji.cn) for editing the English text of a draft of this manuscript.

References

[1] X. Shen, H. Han, Y. Li, C. Yan, D. Mu, A topology optimization based design of space radiator for focal plane assemblies, Energies 14 (19) (2021) 6252, https://doi.org/10.3390/en14196252.

[2] G. Fan, B. Duan, Y. Zhang, X. Ji, S. Qian, Thermal control strategy of OMEGA SSPS based simultaneous shape and topology optimization of butterfly wing radiator, Int. Commun. Heat Mass Tran. 119 (2020), 104912, https://doi.org/10.1016/j.icheatmasstransfer.2020.104912.

[3] A.P.C. Cuco, F.L. de Sousa, V.V. Vlassov, A.J. da Silva Neto, Multi-objective design optimization of a new space radiator, Optim. Eng. 12 (3) (2011) 393–406, https://doi.org/10.1007/s11081-011-9142-6.

[4] K.F.C.H. Sam, Z. Deng, Optimization of a space based radiator, Appl. Therm. Eng. 31 (14–15) (2011) 2312–2320, https://doi.org/10.1016/j.applthermaleng.2011.03.029.

[5] H.-k. Kim, S. Choi, S.-O. Park, Kyun Ho Lee, Node-based spacecraft radiator design optimization, Adv. Space Res. 55 (5) (2015) 1445–1469, https://doi.org/10.1016/j.asr.2014.09.007.

[6] M. Bulut, N. Sözbir, Optimized analytical solution of platform panel radiative area dimensioning of geostationary communications satellites: a practical approach, Sakarya University Journal of Science 23 (5) (2019) 986–992, https://doi.org/10.16984/saufenbilder.546894.

[7] M. Bulut, N. Sözbir, A novel approach to estimating dimensions of three-axis stabilized communication satellites with optimal heat transfer, J. Therm. Anal. Calorim. (2023), https://doi.org/10.1007/s10973-022-11933-0.

[8] R.D. Vilela, E.C. Garcia, Numerical model for analysis in space radiators for critical conditions operating, International Review of Mechanical Engineering (IREME) 8 (5) (2014), https://doi.org/10.15866/ireme.v8i5.2063.

[9] C. Arslanturk, Optimization of space radiators accounting for variable thermal conductivity and base-to-fin radiation interaction, Proc. Inst. Mech. Eng. G J. Aerosp. Eng. 232 (1) (2016) 121–130, https://doi.org/10.1177/0954410016673091.

[10] H. Öktem, T. Erzurumlu, H. Kurtaran, Application of response surface methodology in the optimization of cutting conditions for surface roughness, J. Mater. Process. Technol. 170 (1–2) (2005) 11–16, https://doi.org/10.1016/j.jmatprotec.2005.04.096.

[11] H.-S. Park, N.H. Pham, Design of conformal cooling channels for an automotive part, Int. J. Automot. Technol. 10 (1) (2009) 87–93, https://doi.org/10.1007/s12239-009-0011-7.

[12] K. Dehghani, A. Nekahi, M.A.M. Mirzaie, Optimizing the bake hardening behavior of Al7075 using response surface methodology, Mater. Des. 31 (4) (2010) 1768–1775, https://doi.org/10.1016/j.matdes.2009.11.014.

[13] Y.-Y. Chen, J.T. Lin, A modified particle swarm optimization for production planning problems in the TFT Array process, Expert Syst. Appl. 36 (10) (2009) 12264–12271, https://doi.org/10.1016/j.eswa.2009.04.072.

[14] M.A. Bezerra, R.E. Santelli, E.P. Oliveira, L.S. Villar, L.A. Escaleira, Response surface methodology (RSM) as a tool for optimization in analytical chemistry, Talanta 76 (5) (2008) 965–977, https://doi.org/10.1016/j.talanta.2008.05.019.

[15] S.C. Ferreira, R. Bruns, H.S. Ferreira, G.D. Matos, J. David, G. Brandão, E.P. da Silva, L. Portugal, P. Dos Reis, A. Souza, Box-Behnken design: an alternative for the optimization of analytical methods, Anal. Chim. Acta 597 (2) (2007) 179–186, https://doi.org/10.1016/j.aca.2007.07.011.

[16] M.H. Esfe, O. Mahian, M.H. Hajmohammad, S. Wongwises, Design of a heat exchanger working with organic nanofluids using multi-objective particle swarm optimization algorithm and response surface method, Int. J. Heat Mass Tran. 119 (2018) 922–930, https://doi.org/10.1016/j.ijheatmasstransfer.2017.12.009.

[17] A. Kazemian, M. Khatibi, T. Ma, Performance prediction and optimization of a photovoltaic thermal system integrated with phase change material using response surface method, J. Clean. Prod. 290 (2021), 125748, https://doi.org/10.1016/j.jclepro.2020.125748.

[18] M. Mäkelä, Experimental design and response surface methodology in energy applications: a tutorial review, Energy Convers. Manag. 151 (2017) 630–640, https://doi.org/10.1016/j.enconman.2017.09.021.

[19] M. Rahimi, R. Beigzadeh, M. Parvizi, S. Eiamsa-ard, GMDH-type neural network modeling and genetic algorithm-based multi-objective optimization of thermal and friction characteristics in heat exchanger tubes with wire-rod bundles, Heat Mass Tran. 52 (8) (2016) 1585–1593, https://doi.org/10.1007/s00231-015-1681-5.

[20] J. Zhang, H. Han, Q. Zhu, Multi-objective optimization of the cooling performance of a mini-channel with boot-shaped ribs in transcritical regions using RSM and MOGA, Numer. Heat Tran., Part A: Applications 78 (12) (2020) 737–755, https://doi.org/10.1080/10407782.2020.1805229.